# Reliability of using vegetation optical depth for estimating decadal and interannual carbon dynamics

Yujie Dou, Feng Tian, Wigneron J.-P., Rasmus Fensholt, Torbern Tagesson, Jinyang Du, Martin Brandt, Yi Liu, Linqing Zou, John S Kimball

Remote Sensing of Environment 285 (2023) 113390

Contents lists available at ScienceDirect

Remote Sensing of Environment

journal homepage: www.elsevier.com/locate/rse

# Reliability of using vegetation optical depth for estimating decadal and interannual carbon dynamics

Yujie Dou [a], Feng Tian [a,b,*], Jean-Pierre Wigneron [c], Torbern Tagesson [d,e], Jinyang Du [f], Martin Brandt [e], Yi Liu [g], Linqing Zou [a], John S. Kimball [f], Rasmus Fensholt [e]

[a] Hubei Key Laboratory of Quantitative Remote Sensing of Land and Atmosphere, School of Remote Sensing and Information Engineering, Wuhan University, Wuhan, China
[b] Hubei Luojia Laboratory, Wuhan, China
[c] INRAE, UMR1391 ISPA, Université de Bordeaux, F-33140 Villenave d'Ornon, France
[d] Department of Physical Geography and Ecosystem Science, Lund University, Lund, Sweden
[e] Department of Geosciences and Natural Resource Management, University of Copenhagen, Copenhagen, Denmark
[f] Numerical Terradynamic Simulation Group, W.A. Franke College of Forestry and Conservation, the University of Montana, Missoula, MT 59812, USA
[g] School of Civil and Environmental Engineering, University of New South Wales, Sydney, NSW 2052, Australia

ARTICLE INFO

Edited by Jing M. Chen

*Keywords:*
Vegetation optical depth
Carbon dynamics
Satellite passive microwave
Eddy covariance
Data evaluation

ABSTRACT

Vegetation optical depth (VOD) from satellite passive microwave sensors has enabled monitoring of aboveground biomass carbon dynamics by building a relationship with static carbon maps over space and then applying this relationship to VOD time series. However, uncertainty in this relationship arises from changes in water stress, as VOD is mainly determined by vegetation water content, which varies at diurnal to interannual scales, and depends on changes in both biomass and relative moisture content. Here, we studied the reliability of using VOD from various microwave frequencies and temporal aggregation methods for estimating decadal biomass carbon dynamics at the global scale. We used the VOD diurnal variations to represent the magnitude of vegetation water content buffering caused by climatic variations for a constant amount of dry biomass carbon. This magnitude of VOD diurnal variations was then used to evaluate the likelihood of VOD decadal variations in reflecting decadal dry biomass carbon changes. We found that SMOS-IC L-VOD and LPDR X-VOD can be reliably used to estimate decadal carbon dynamics for 76.7% and 69.9% of the global vegetated land surface, respectively, yet cautious use is warranted for some areas such as the eastern Amazon rainforest. Moreover, the annual VOD aggregated from the 95% percentile of the nighttime VOD retrievals was proved to be the most suitable parameter for estimating decadal biomass carbon dynamics among the temporal aggregation methods. Finally, we validated the use of annual VOD for estimating interannual carbon dynamics by comparing VOD changes between adjacent years against eddy covariance estimations of gross primary production from flux sites over several land cover classes across the globe. Despite the large difference in spatial scales between them, the positive correlation obtained supports the capability of satellite VOD in quantifying interannual carbon dynamics.

## 1. Introduction

Land carbon fluxes play a dominant role in controlling the interannual variability of atmospheric carbon dioxide (Friedlingstein et al., 2020). Currently, estimations of interannual variability of global carbon stocks are mainly based on process-based dynamic vegetation models, yet large spatiotemporal divergence is observed between different models (Piao et al., 2020). Optical remote sensing is sensitive to the green foliar component thereby well suited for estimating biomass of herbaceous vegetation, but not for forest ecosystems where the leaf component only accounts for a small fraction of the biomass carbon pool. Aerial and spaceborne light detection and ranging (LiDAR), low-frequency synthetic aperture radar (SAR), and global ecosystem dynamics investigation (GEDI) provide information on tree height and thus biomass carbon in forests, but yet at limited spatial and temporal coverage (Baccini et al., 2012; Dubayah et al., 2020; Duncanson et al.,

* Corresponding author at: Hubei Key Laboratory of Quantitative Remote Sensing of Land and Atmosphere, School of Remote Sensing and Information Engineering, Wuhan University, Wuhan, China.
*E-mail address:* tian.feng@whu.edu.cn (F. Tian).

https://doi.org/10.1016/j.rse.2022.113390
Received 19 May 2022; Received in revised form 16 November 2022; Accepted 20 November 2022
Available online 30 November 2022

2022; Lang et al., 2022; Liu et al., 2015; Ni-Meister et al., 2022; Yu and Saatchi, 2016).

Recently, satellite passive microwave remote sensing has further advanced our abilities by providing the means for monitoring annual carbon dynamics at continental to global scales through vegetation optical depth (VOD) (Brandt et al., 2018; Fan et al., 2019; Liu et al., 2015; Santi et al., 2012; Scholze et al., 2019; Vaglio Laurin et al., 2020; Wigneron et al., 2020). VOD is a parameter used for quantifying microwave transmissivity of the vegetation layer and is mainly determined by vegetation water content (VWC) from both foliar and woody components (Cui et al., 2015; Shi et al., 2008; Tian et al., 2017, 2018). Annual aggregated VOD data have shown strong spatial relationships with static tree height and carbon estimations at local, continental, and global scales (Brandt et al., 2018; Chaparro et al., 2019; Liu et al., 2015; Rodríguez-Fernández et al., 2018; Vittucci et al., 2019). Therefore, for the estimation of interannual carbon dynamics, a common practice is to build an empirical relationship between annual VOD data and static carbon maps (Baccini et al., 2012; Saatchi et al., 2011) over space and then apply this relationship on annual VOD time series. An underlying assumption behind this practice is that the ratio between wet and dry biomass, or the plant water-holding capacity, remains constant across years.

However, this assumption could be potentially unfulfilled due to vegetation physiological responses to climate variations. For example, recent studies showed that VOD retrievals from in situ microwave radiometers convey climate-induced changes in plant water potential (Holtzman et al., 2021) and it is critical to distinguish between water stress and biomass dynamics in their contributions to VOD changes (Konings et al., 2021a). Moreover, the radiative transfer process for a vegetated land surface is highly complex and uncertainties often arise from a simplification of the algorithms used for retrieving VOD from the same satellite observation (Wigneron et al., 2021). The impacts of these confounding factors are difficult to evaluate due to the large spatial footprint of space-borne microwave radiometers and also the lack of temporally continuous and field-measured biomass data at large scales, particularly for forest areas. Only Tian et al. (2016) evaluated a satellite-based VOD dataset with ground-measured green biomass from the African Sahel grassland/savanna over two decades, but this did not include substantial amounts of wood biomass. Recently, Qin et al. (2021) evaluated a VOD dataset by comparing it with forest cover change in the Amazonian rainforest. More work is needed to evaluate the capability of VOD changes in reflecting the interannual variability of biomass carbon for various land cover types across the globe.

Eddy covariance flux towers continuously measure the net ecosystem exchanges (NEE) of carbon dioxide between the land and the atmosphere and partition it into ecosystem respiration and gross primary production (GPP) at relatively high accuracy (Moncrieff et al., 1996; Pastorello and Hörtnagl, 2020; Tagesson et al., 2016). For regions with relatively homogeneous vegetation conditions and with little disturbances, interannual changes in eddy covariance carbon fluxes at the site level could be representative of the climate-related biomass carbon variations in the surrounding region. Thereby, eddy covariance measurements could be potentially used for estimating the VOD reliability in representing the interannual carbon dynamics.

Microwave radiometers onboard polar-orbiting satellites provide day-and-night measurements with 1–3 day global coverage. This high temporal frequency is critical for studying plant hydraulics (Konings and Gentine, 2017), but for the estimation of biomass carbon dynamics, the daily VOD retrievals need to be aggregated to an annual scale to reduce the influence of the water-related diurnal and seasonal phenology changes in plants. Various annual VOD indices (i.e. strategies for temporal aggregation) have been applied in previous studies, including taking the median or mean value of high-quality daily VOD retrievals for each year (Brandt et al., 2018; Fan et al., 2019; Frappart et al., 2020; Teubner et al., 2019) and taking the 95% percentile (Qin et al., 2021). Apart from the different ways of conducting temporal aggregation, the input daily VOD retrievals have also been used differently by either applying data from nighttime (Brandt et al., 2018; Liu et al., 2015; Qin et al., 2021) or the combination of both daytime and nighttime (Fan et al., 2019). Yet, there is currently no consensus about how temporal aggregation of VOD data should be carried out when being used for monitoring decadal carbon dynamics.

In this study, we aim to evaluate the reliability of using VOD data for inferring biomass carbon dynamics at decadal and interannual scales by evaluating water stress impacts using VOD diurnal changes, and by using global eddy covariance carbon flux measurements over multiple years, respectively. We also examined the performance of various temporal aggregation methods for obtaining annual VOD values from the original quasi-daily observations for carbon dynamics estimation.

## 2. Data

Microwaves can penetrate through the vegetation canopy, and lower frequency or longer wavelength has deeper penetration depth. Here, we examined VOD products at three frequencies, including L-VOD (1.4 GHz) from SMOS-IC (Soil Moisture and Ocean Salinity - INRA-CESBIO), X-VOD (10.7 GHz) from LPDR (Land Parameter Data Record), and X-VOD and Ku-VOD (18.7 GHz) from VODCA (VOD Climate Archive) (Table 1). The C-band VOD data were not considered in this study since (a) only X-band VOD data are available from the LPDR data set for mitigating the impacts of radio frequency interference (RFI) (Du et al., 2017; Njoku et al., 2005), and (b) the VODCA C-band product has relatively higher data loss and lower accuracy than X- and Ku-band data (Moesinger et al., 2020).

The SMOS-IC L-VOD was retrieved from temperature brightness (TB) observed from the SMOS satellite using the inversion of the L-MEB (L-band Microwave Emission of the Biosphere) model (Fernandez-Moran et al., 2017; Wigneron et al., 2021), and provides L-VOD data at two overpassing times a day at 6:00 AM (referred to as nighttime) and 6:00 PM (referred to as daytime) local time, respectively. At L-band, RFI strongly affects the SMOS TB observations and the Root Mean Square Error (RMSE) value between the observed and the L-MEB modeled TB (TB-RMSE), which has often been used to filter out VOD data which are strongly affected by RFI effects. In this study, we retain pixels with TB-RMSE $<8$ K as suggested by Wigneron et al. (2021). The SMOS-IC VOD dataset is publicly available from https://ib.remote-sensing.inrae.fr/.

The semi-daily global LPDR X-VOD (Version 3) dataset was derived from AMSR-E (the Advanced Microwave Scanning Radiometer - Earth Observing System) and AMSR-2 (the Advanced Microwave Scanning Radiometer - 2) sensors (Du et al., 2017) with two observations a day at 1:30 AM (descending orbit, referred to as nighttime) and 1:30 PM (ascending orbit, referred to as daytime) local time, respectively. The LPDR VOD dataset is publicly available from https://nsidc.org/data/nsidc-0451.

The VODCA dataset combines VOD retrievals derived from multiple sensors, including SSM/I (Special Sensor Microwave/Imager), TMI (Tropical Rainfall Measuring Mission's Microwave Imager), AMSR-E, AMSR-2, and WindSat (Moesinger et al., 2020). X-VOD and Ku-VOD provided by VODCA were used in this study and downloaded from https://doi.org/10.5281/zenodo.2575599.

We collected eddy covariance GPP data from three publicly available networks, including FLUXNET2015 (https://fluxnet.org/), ICOS (https://www.icos-cp.eu/), and ONEFLUX (https://ameriflux.lbl.gov/), resulting in an eddy covariance dataset containing 251 sites with 1877 site-years spanning from 1991 to 2018 across the globe (Fig. 1).

Besides VOD data and flux measurements, we also used four ancillary datasets, including transpiration, Moderate-resolution Imaging Spectroradiometer (MODIS) vegetation index, MODIS land cover, and Copernicus land cover. The Global Land Evaporation Amsterdam Model (GLEAM) product (Version 3) provides daily global transpiration with one-quarter degree spatial resolution (Martens et al., 2016; Miralles et al., 2011) and is publicly available at https://www.gleam.eu/. It

**Table 1**
VOD products used in this study. All of the datasets were gridded at one-quarter degree. The SMOS-IC and LPDR products provide VOD retrievals for two overpassing times per day, while the VODCA product merges the two overpassing times into one observation per day.

| Products | Satellite sensor | Microwave frequency | Maximum temporal resolution | Overpassing time | Timespan | Reference |
|---|---|---|---|---|---|---|
| SMOS-IC | SMOS | L-band | Semi-daily | 6:00 AM (ascending)<br>6:00 PM (descending) | 2011–2019 | Wigneron et al. (2021) |
| LPDR | AMSR-E, AMSR-2 | X-band | Semi-daily | 1:30 AM (descending)<br>1:30 PM (ascending) | 2003–2019 | Du et al. (2017) |
| VODCA | TMI, AMSR-E, AMSR-2, Windsat | X-band | Daily | / | 1998–2018 | Moesinger et al. (2020) |
| VODCA | SSM/I, TMI, AMSR-E, AMSR-2, Windsat | Ku-band | Daily | / | 1988–2016 | Moesinger et al. (2020) |

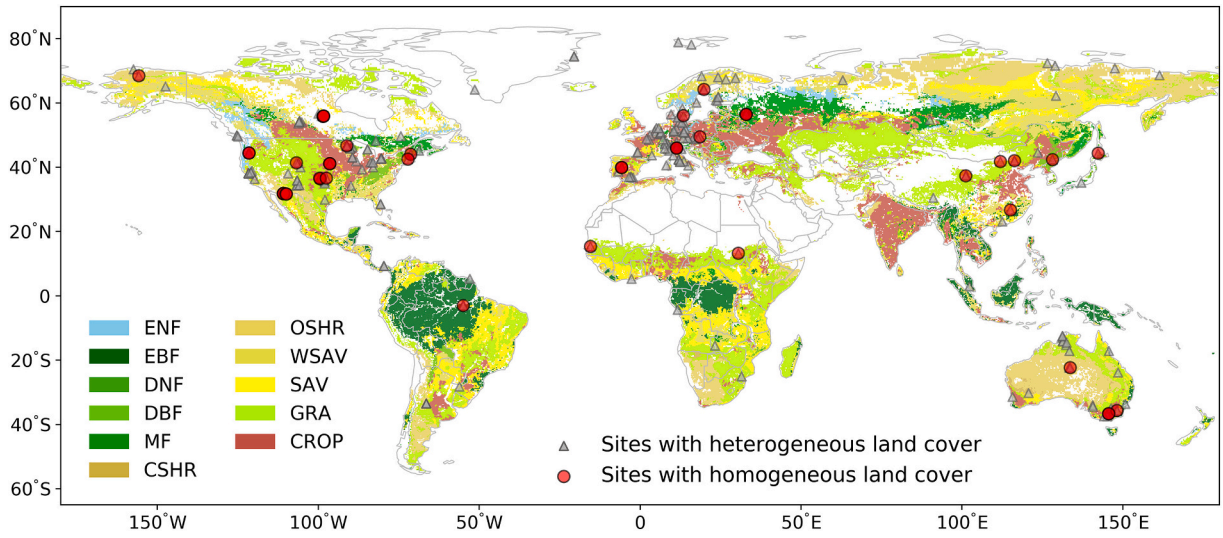


**Fig. 1.** Locations of the eddy covariance flux sites superimposed on the MODIS land cover classes. The procedures for determining sites surrounded by homogenous or heterogeneous land cover classes are explained in Section 3.3. ENF: Evergreen Needleleaf Forests, EBF: Evergreen Broadleaf Forests, DNF: Deciduous Needleleaf Forests, DBF: Deciduous Broadleaf Forests, MF: Mixed Forests, CSHR: Closed Shrublands, OSHR: Open Shrublands, WSAV: Woody Savannas, SAV: Savannas, GRA: Grasslands, CROP: Croplands.

contains a set of algorithms designed to estimate different components of terrestrial evapotranspiration from satellite data, including transpiration, bare-soil evaporation, open-water-evaporation et al.

The MODIS Enhanced Vegetation Index (EVI) data from the MOD13A1 / MYD13A1 V6.0 product (Didan, 2015) at a 16-day temporal interval and 500 m spatial resolution was used to verify whether a flux site is representative of the vegetation conditions over the VOD footprint encompassing the tower (see Section 3.3 for more details). To match with the VOD data, MODIS EVI was spatially aggregated to one-quarter degree by averaging. Data was also temporally aggregated to annual time series from 2011 to 2019 by taking the median values.

The MODIS land cover type data (MCD12Q1) obtained in 2018 provides a suite of datasets that map global land cover at 500 m spatial resolution (Friedl et al., 2019). The commonly used International Geosphere-Biosphere Program (IGBP) classification scheme was used in this study.

The Copernicus global land cover product obtained in 2018 has been generated at 100 m spatial resolution using PROBA-V observations as inputs (Buchhorn et al., 2020). The higher spatial resolution of Copernicus land cover as compared to MODIS land cover is beneficial for quantifying the homogeneity of eddy covariance sites at the VOD footprint, while MODIS land cover was used for calculating statistics in the analysis.

## 3. Methodology

The data analyses were performed in three parts (Fig. 2), which are described in the following sections.

### 3.1. Relating $\Delta VOD_{day}$ to transpiration

Water transportation through the soil-plant-atmosphere continuum is driven by the gradient of water potential from root-soil interface to leaf-atmosphere interface (Lincoln Taiz, 2014). When leaf stomata open during the daytime, plant water loss through transpiration is usually faster than root-soil water absorption, leading to a water deficit in the plants (Konings et al., 2021b). During nighttime after sunset, the leaf stomata generally close and transpiration stops, and the plant water deficit is replenished by soil water uptake (Dawson et al., 2007). Thus, VWC buffers the imbalance between transpiration water loss and soil water supply (Daly et al., 2004).

With a semi-daily frequency (Table 1), satellite VOD retrievals could be used to measure VWC diurnal changes ($\Delta VOD_{day}$, nighttime VOD minus daytime VOD), thus representing plant water deficit associated with transpiration during daytime. We verified this assumption by examining the relationship between $\Delta VOD_{day}$ and transpiration in our analysis.

The satellite revisit frequency for each overpass (nighttime or daytime) varies from one day in the polar regions to three days at the Equator (Fig. S1). Thus, to ensure continuous spatial coverage, the VOD raw data were combined into 8-day composites (also considering data gaps due to low data quality) by averaging daytime and nighttime observations separately (Fig. S2). The $\Delta VOD_{day}$ was calculated as the VOD difference between the nighttime and daytime 8-day composites. To enable temporal consistency, the daily GLEAM transpiration data was also aggregated to an 8-day interval of the same days with valid VOD retrievals by averaging. We then compared the 8-day composited

**VOD and eddy covariance data processing**
8-day composites daytime and nighttime VOD calculation; annual VOD calculation; the selection of homogeneous flux sites and annual GPP calculation.

**Section 3.1** (Examines at 8-day temporal scale) Examines the relationship between transpiration and VOD diurnal difference to verify that diurnal VOD variation could be used to measure vegetation water content variation.

**Section 3.2** (Compares at decadal scale) Takes average VOD diurnal difference as the threshold of diurnal plant water buffering. Compares average VOD diurnal difference and VOD decadal variations to estimate the likelihood of VOD decadal variation in reflecting decadal biomass carbon dynamics at global scale.

**Section 3.3** (Examines at interannual scale) Examines relationship between annual GPP and the VOD differences between successive years to validate the reliability of using annual VOD for estimating interannual carbon dynamics.

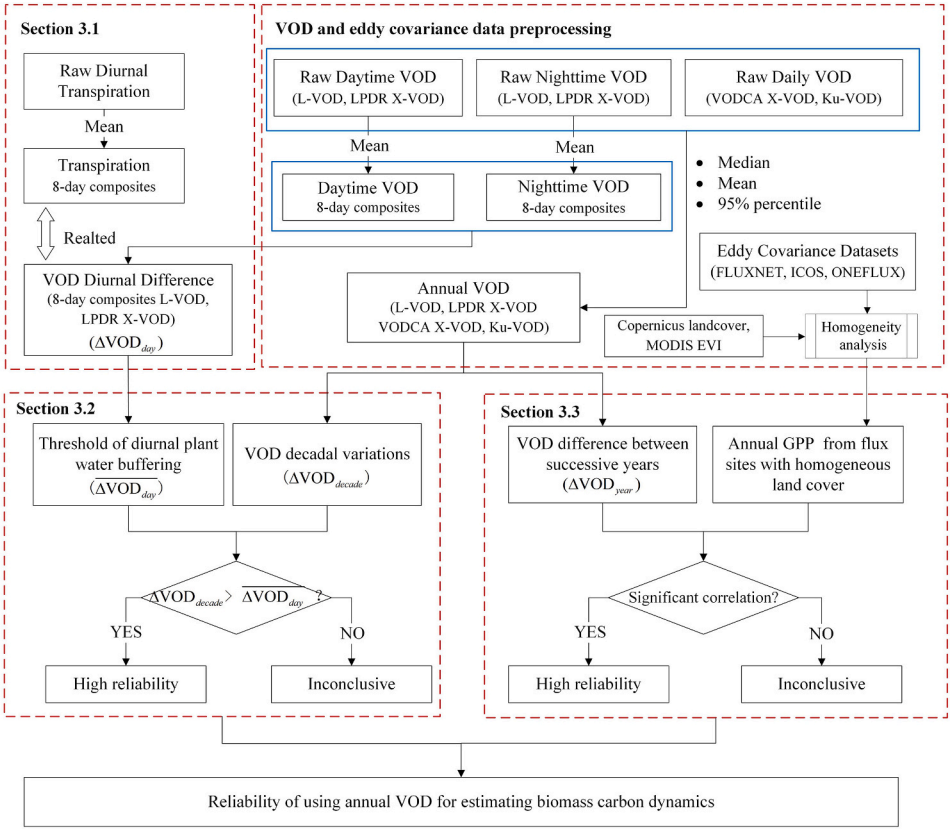


**Fig. 2.** Workflow and overall structure of the study.

$\Delta VOD_{day}$ and transpiration at pixel level during 2011–2019 by calculating Pearson's correlation (Fig. 2). If $\Delta VOD_{day}$ was positively correlated with transpiration, we hypothesized that for a given pixel, $\Delta VOD_{day}$ could represent the magnitude of water content variations driven by climatic conditions for a constant amount of dry biomass carbon.

### 3.2. Evaluating VOD for estimating decadal biomass carbon dynamics

VOD is determined by VWC (Liu et al., 2011), and affected by both water stress conditions (Konings et al., 2019; Zhang et al., 2019) and biomass (Momen et al., 2017). Diurnal VOD changes are used to evaluate the water stress impacts (Rao et al., 2019) while biomass dynamics are likely being inferred from long-term VOD observations after minimizing the diurnal water stress impacts (Brandt et al., 2018; Fan et al., 2019; Qin et al., 2021). Thus, we evaluated VOD changes at different time scales (e.g. sub-daily and decadal) for minimizing the water stress impacts on VOD-based biomass estimation by introducing a threshold of VWC-driven average VOD diurnal changes ($\overline{\Delta VOD_{day}}$) that is compared with $\Delta VOD_{decade}$.

$\Delta VOD_{decade}$ was calculated as the maximum variation of the aggregated annual VOD (i.e. the maximum annual VOD minus the minimum annual VOD) during the entire studied period (Supplementary Figs. S3-S4). There were six methods typically used to derive annual VOD from the raw data that have been identified in the literature, including taking the median, mean, and 95% percentile values from nighttime VOD and the combination of daytime and nighttime VOD, respectively. We tested all six different approaches, and for any given pixel, the aggregated annual VOD was built by at least 30 daily observations as suggested by Wigneron et al. (2021).

Plants regulate the leaf and xylem water potentials at a relatively safe range by controlling the stomatal conductance (Meinzer et al., 2009) to prevent hydraulic failure under varying climatic conditions, especially in dry conditions when an excessively negative water potential within the plants can cause xylem embolism and put the plants at high risk of hydraulic failure (Momen et al., 2017). Thus, there should be a threshold to represent the magnitude of the intrinsic variability of VWC. $\Delta VOD_{day}$ varies over the course of the year driven by both external climatic conditions and plant traits, such as the number of green leaves, the age of the leaves, and the plant's hydraulic regulation strategies (Konings et al., 2017; Konings and Gentine, 2017). For example, isohydric species tend to have relatively constant plant water content under water stress, thus the $\Delta VOD_{day}$ remains relatively constant during the course of the year. By contrast, anisohydric species keep their stomata open longer, allowing for higher photosynthetic rates, but also causing increased rates of transpiration. This causes large annual fluctuation in plant water content with higher values during the growing season (Fig. 3), also causing substantial fluctuations in the $\Delta VOD_{day}$ for these species (Konings and Gentine, 2017). Moreover, when VOD is being used for estimating decadal scale carbon dynamics and minimizing the impacts of sub-daily VWC variations, the original semi-daily VOD observations were often aggregated to annual VOD statistics by using the mean, median, or 95% percentile. Thus, to make $\Delta VOD_{day}$ comparable to these commonly used annual VOD statistics, we used the average VOD diurnal changes ($\overline{\Delta VOD_{day}}$) to represent the magnitude of the intrinsic variability of VWC for each pixel, and considered it as the most suitable parameter to represent the magnitude of VWC buffering caused by climatic and seasonal variations for a constant amount of dry biomass carbon.

We calculated $\overline{\Delta VOD_{day}}$ value by averaging the $\Delta VOD_{day}$ time-series pixel-wise (Fig. 3). As the most pronounced changes happened between the years of the maximum and minimum annual VOD, we restricted the calculation of $\overline{\Delta VOD_{day}}$ to this sub-period (e.g. 2016 to 2019 in Fig. 3, which corresponds to the period of the minimum and maximum annual VOD) instead of the entire studied period to better represent the mean

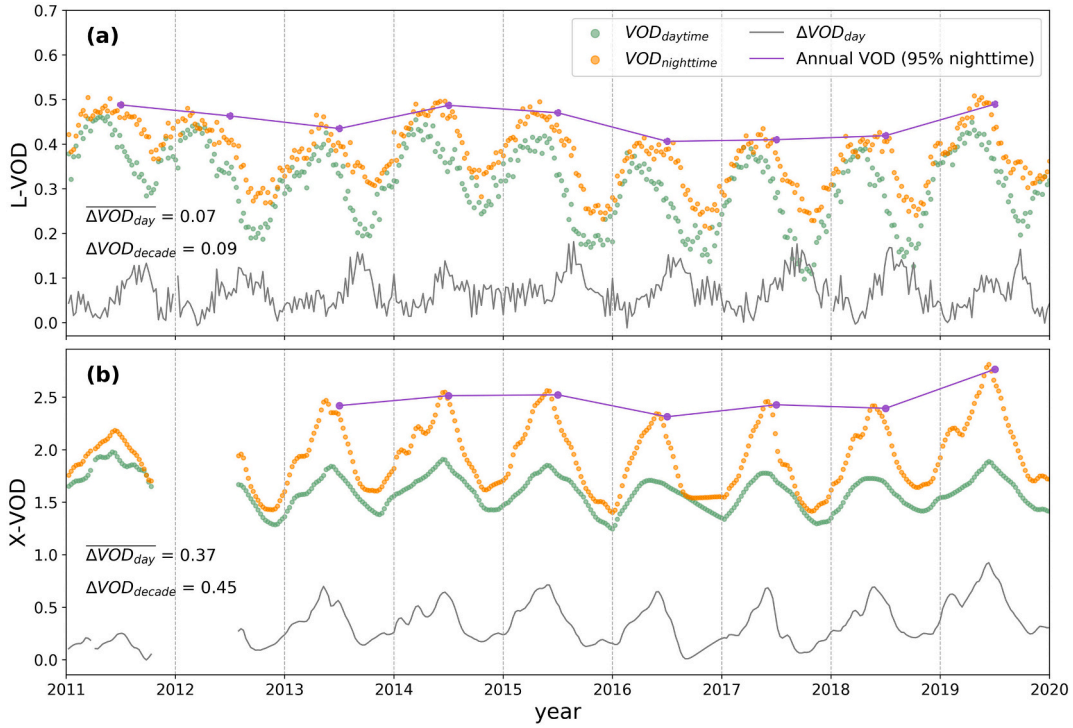


**Fig. 3.** An example of 8-day time series of (a) SMOS-IC L-VOD and (b) LPDR X-VOD diurnal variation over a woodland pixel (6° S, 43.3° W). Note that there is a data gap in LPDR X-VOD during 2011–2012 due to the transition from AMSR-E to AMSR2.

vegetation conditions corresponding to the $\Delta VOD_{decade}$ metric. It is noted that negative $\Delta VOD_{day}$ values, denoting higher daytime VOD than nighttime VOD, are observed in large parts of the world (37% for SMOS-IC L-VOD and 35% for LPDR X-VOD) and here we took the absolute value of $\Delta VOD_{day}$ for calculating $\overline{\Delta VOD_{day}}$ (Supplementary Fig. S5; and the Discussions Section).

We then performed a pixel-wise assessment using $\overline{\Delta VOD_{day}}$ as a threshold to determine whether $\Delta VOD_{decade}$ is dominated by dry biomass changes. Specifically, if $\Delta VOD_{decade}$ is smaller than $\overline{\Delta VOD_{day}}$, the VOD decadal variations are within the plant water buffering range and thus could potentially be attributed to changes in climate conditions with little or no alteration in dry biomass (labeled as inconclusive). If $\Delta VOD_{decade}$ is larger than $\overline{\Delta VOD_{day}}$, VOD decadal variations could not be totally explained by plant water changes and thus are most likely due to changes in dry biomass (labeled as high-reliability) (Fig. 2).

### 3.3. Evaluating VOD for estimating interannual biomass carbon dynamics using eddy covariance

For the assessment of interannual biomass carbon dynamics, one possible way is the use of eddy covariance measurements of GPP at sites representative of larger areas (e.g. 25 km by 25 km satellite footprint) with homogeneous land cover and similar vegetation conditions. Here, Copernicus global land cover data (100 m spatial resolution) and MODIS EVI annual time series (500 m resolution) were used to select flux sites meeting these requirements.

Based on the land cover data, a selected flux site should meet the criteria that (1) the land cover class of the flux tower should be the dominant class and account for more than half of the area covered by the VOD pixel, (2) the area of open water bodies should be <2% of the VOD pixel as open water can significantly affect the VOD retrievals, and (3) the VOD pixel covering a flux site should be at least 25 km away from the coastline. 63 out of the 251 sites met these requirements.

For a flux site covering a homogeneous spatial representation of vegetation cover, the vegetation dynamics at the flux site (footprint radius at about 100–200 m) should be representative of the vegetation conditions and temporal variability over the full VOD pixel (25 km resolution) covering the flux site. To evaluate the representativeness of the flux sites in comparison to the full VOD pixel, the MODIS time series was used as a bridge. Specifically, we compared the EVI interannual variability of the MODIS pixel covering the flux site (500 m resolution, $EVI_{fluxsite}$) to the average of that of the MODIS pixels encompassing the VOD pixel ($EVI_{VOD}$). This was done by calculating Pearson's correlation between the annual time series of $EVI_{fluxsite}$ and $EVI_{VOD}$ ($p < 0.05$ and $R > 0$).

A final selection criterion was that the overlapping period of GPP and VOD time series should be >3 years to ensure at least 3 years of paired $\Delta VOD_{year}$ and GPP for the inter-comparison. In total, 42 flux sites (Fig. 1) were retained for further analysis between $\Delta VOD_{year}$ and GPP. Information on the selected flux sites is shown in Table S1.

GPP is the primary terrestrial carbon sink (Friedlingstein et al., 2020), and about 50% of the GPP is generally considered to be the net carbon sequestrated by the ecosystem (Waring et al., 2016). Therefore, if the annual VOD time series could reflect year-to-year changes in biomass carbon, the VOD difference between successive years ($\Delta VOD_{year}$, following year VOD minus the previous year VOD) would correspond well with GPP. Pearson's correlation coefficient was used to quantify the relationships between GPP and$\Delta VOD_{year}$ for each aggregated annual VOD dataset (Fig. 2). To eliminate the site-related differences (e.g. land cover types) and make various sites comparable, $\Delta VOD_{year}$ and annual GPP time series were standardized at each site by subtracting the mean values and dividing by standard deviations to obtain the *Z*-scores.

The annual GPP values were obtained by summing up the daily data, and the daily data was obtained from the averaged values of daytime GPP (GPP_DT_VUT_REF) and nighttime GPP (GPP_NT_VUT_REF) from the variable USTAR threshold (VUT) method (Pastorello and Hörtnagl, 2020), both of which were all aggregated from half-hour GPP estimates with good quality (QC < 1).

## 4. Results

### 4.1. Relationship between $\Delta VOD_{day}$ and transpiration

The diurnal variations in SMOS-IC L-VOD are moderately consistent with the transpiration data with 39% of the global vegetated land surface showing a significantly positive relationship ($p < 0.05$) during 2011–2019 (Fig. 4a). The majority of these pixels are located in regions with a pronounced seasonality, including the African dry and subhumid regions, the Brazilian Cerrado, North America, the northern and eastern parts of Europe, the deciduous boreal forest in northern Russia, and open savanna regions in Australia (Fig. 4a). Significantly positive correlation between diurnal variation in LPDR X-VOD and transpiration is obtained for 92% of the global vegetated land surface (Fig. 4b). The regions with significantly negative or insignificant relationships were mainly distributed in tropical forests. The moderate and significant correlations between $\Delta VOD_{day}$ and transpiration for L-VOD and X-VOD, respectively suggest that $\Delta VOD_{day}$ can represent plant water deficit associated with transpiration during the daytime, and therefore $\Delta VOD_{day}$ can be used to measure VWC diurnal changes.

### 4.2. Reliability of using VOD for decadal biomass carbon dynamics

High-reliability ($\Delta LVOD_{decade} > \overline{\Delta LVOD_{day}}$) pixels for L-VOD are dominating across the global vegetated surface for all six tested temporal aggregation approaches of producing annual VOD from daily observations (Fig. 5). However, differences are evident among the approaches, with the largest area of high-reliability pixels (76.7% of the global vegetated surface) from using the 95% percentile of the nighttime (6:00 AM) L-VOD (Fig. 5a), and the smallest area (53.6% of the global vegetated surface) from using the mean value of combined daytime and nighttime L-VOD (Fig. 5f). The pixels defined as inconclusive for L-VOD to estimate interannual biomass dynamics are observed mainly in southeastern Russia, China, tropical rainforests in the east Amazon, eastern Europe, and western Australia (Fig. 5a).

For LPDR X-VOD, the method of annual aggregation by taking the 95% percentile of the nighttime X-VOD is consistently superior to the other methods across the vegetated land surface (Fig. 6). However, the numbers of high-reliability pixels based on X-VOD are much lower than those for SMOS-IC L-VOD (Fig. 5) with the areal proportions of high-reliability pixels ranging from 48.1% (median value of combined daytime and nighttime VOD) to 69.9% (95% percentile method) (Fig. 6). For X-VOD, most of the humid forest areas are inconclusive in estimating interannual biomass carbon dynamics, such as in the tropical rainforest areas, while drylands dominated by shrublands and herbaceous vegetation showed high reliability in representing interannual carbon dynamics.

We summarized the percentage of high-reliability pixels for L-VOD and LPDR X-VOD across different MODIS landcover classes (Fig. 7). Both L-VOD and LPDR X-VOD show relatively high percentages (> 80% at most) in grasslands (GRA), and open shrublands (OSHR) regions. However, large variability is seen between different annual VOD

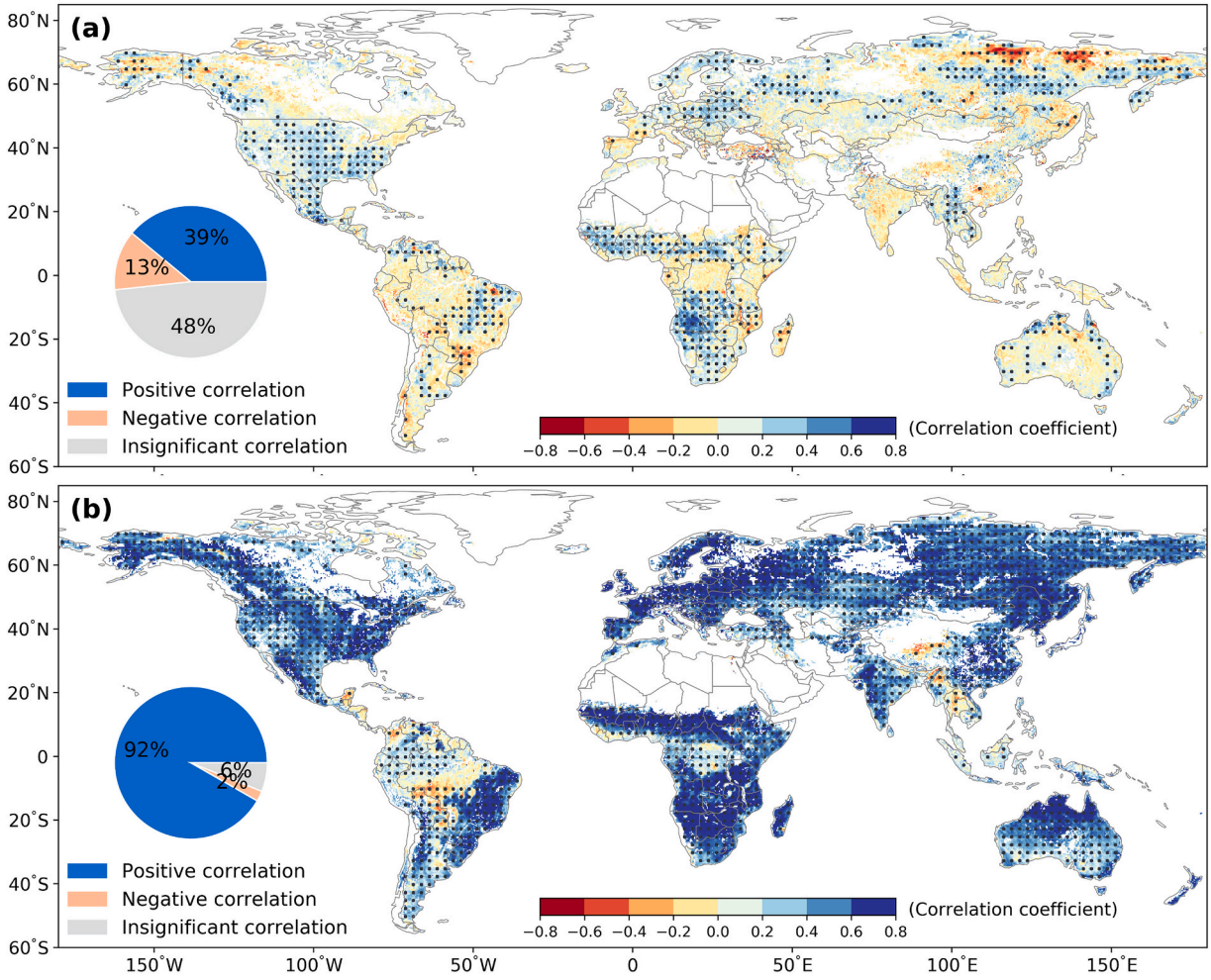


**Fig. 4.** Relationship between $\Delta VOD_{day}$ and transpiration for (a) SMOS-IC L-VOD and (b) LPDR X-VOD. Regions labeled by black dots indicate statistically significant ($p < 0.05$) correlation coefficients.

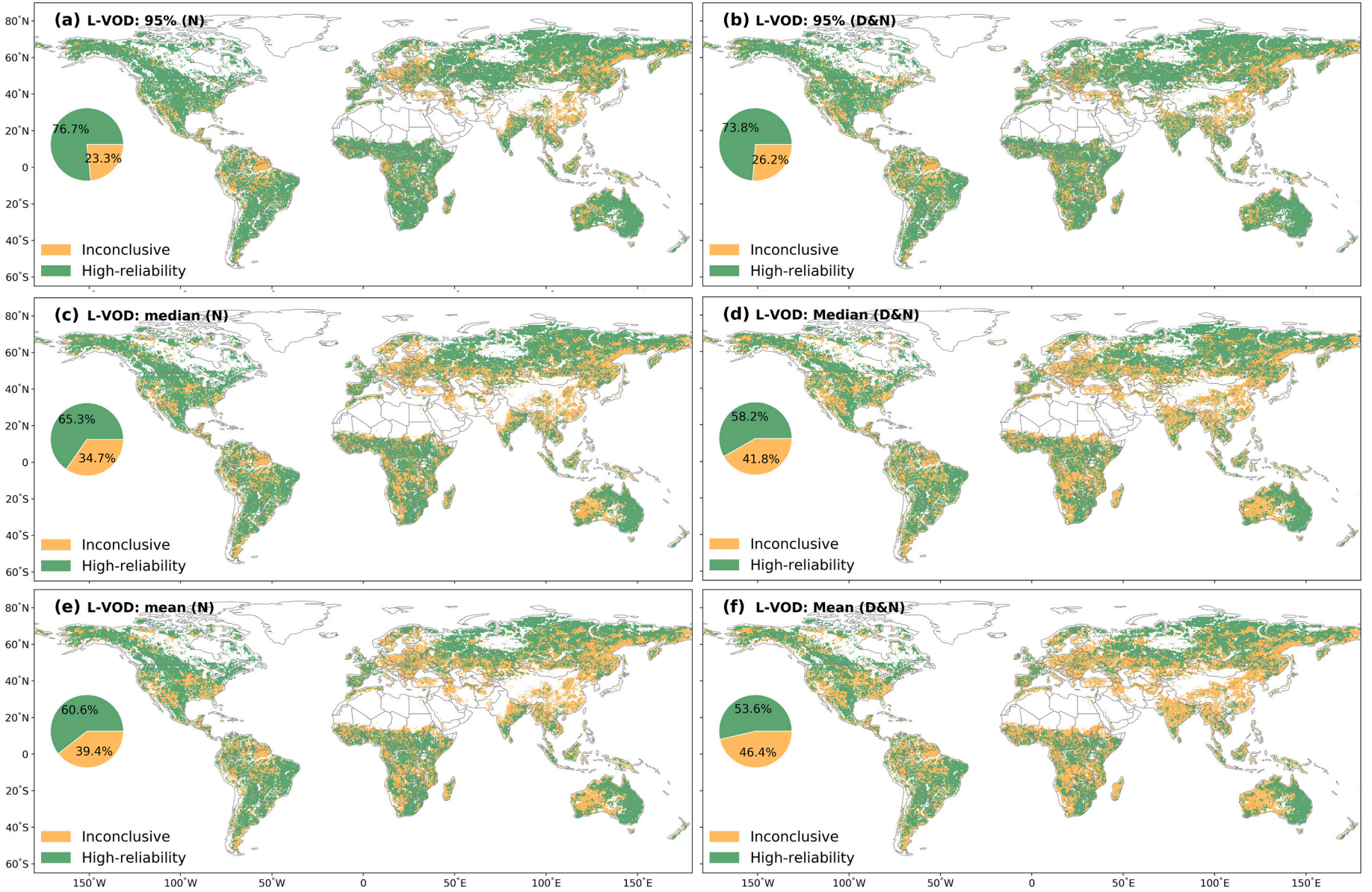


**Fig. 5.** Comparison between $\overline{\Delta LVOD_{day}}$ and $\Delta LVOD_{decade}$ using different approaches for annual aggregation. The annual VOD values were retrieved from (a) 95% percentile of nighttime VOD, (b) 95% percentile of combined daytime and nighttime VOD, (c) median of nighttime VOD, (d) median of combined daytime and nighttime VOD, (e) mean of nighttime VOD, and (f) mean of combined daytime and nighttime VOD.

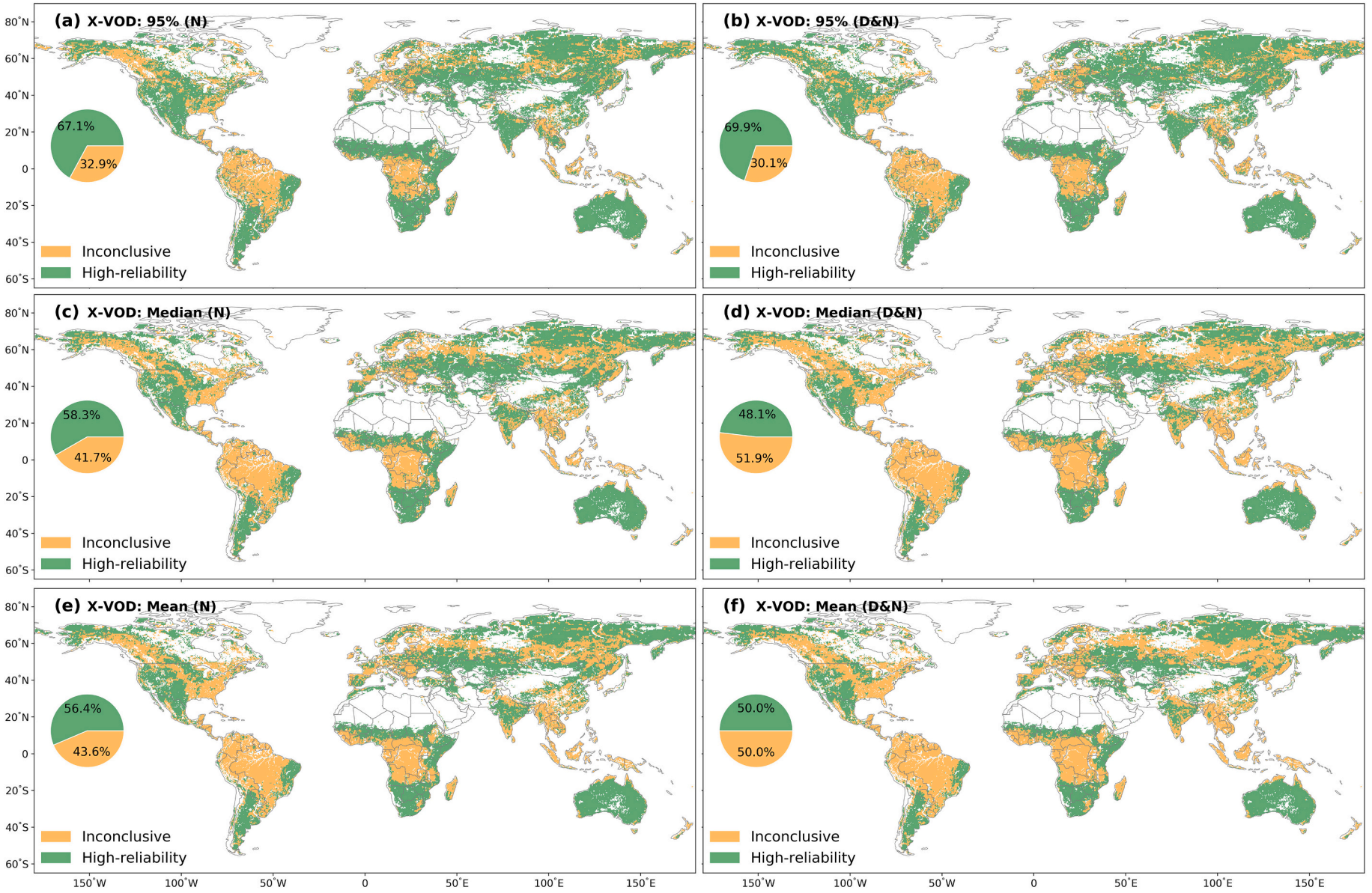


**Fig. 6.** Comparison between $\overline{\Delta XVOD_{day}}$ and $\Delta XVOD_{decade}$ using different approaches for annual aggregation. The annual VOD values were retrieved from (a) 95% percentile of nighttime VOD, (b) 95% percentile of combined daytime and nighttime VOD, (c) median of nighttime VOD, (d) median of combined daytime and nighttime VOD, (e) mean of nighttime VOD, and (f) mean of combined daytime and nighttime VOD.

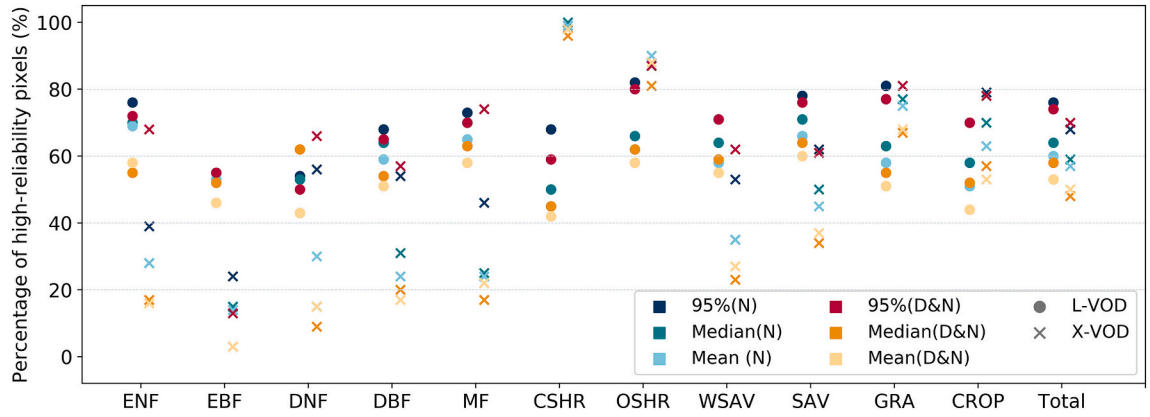


**Fig. 7.** Statistics of the percentage of high-reliability pixels over different MODIS IGBP land cover classes for SMOS-IC L-VOD and LPDR X-VOD. "D" indicates the daytime VOD, and "N" represents the nighttime VOD. ENF: Evergreen Needleleaf Forests, EBF: Evergreen Broadleaf Forests, DNF: Deciduous Needleleaf Forests, DBF: Deciduous Broadleaf Forests, MF: Mixed Forests, CSHR: Closed Shrublands, OSHR: Open Shrublands, WSAV: Woody Savannas, SAV: Savannas, GRA: Grasslands, CROP: Croplands.

generation methods. L-VOD clearly outperforms LPDR X-VOD for tree-dominating ecosystems, such as evergreen broadleaf forests (mean 53% vs. 12%), deciduous broadleaf forests (mean 60% vs. 34%), woody savannas (mean 63% vs. 39%), and savannas (mean 69% vs. 48%). Contrastingly, LPDR X-VOD shows higher percentages of high-reliability pixels than L-VOD for closed shrublands (mean 98% vs. 52%) and open shrublands (mean 87% vs. 68%).

### 4.3. Reliability of using VOD for interannual biomass carbon dynamics

The correlation coefficients between standardized $\Delta VOD_{year}$ and GPP time series vary among VOD products and annual VOD aggregation methods (Figs. 8-9), but positive relationships between $\Delta VOD_{year}$ and GPP are obtained for all of the VOD datasets examined when using all sites and all years together (Figs. 8 and 9a). For SMOS-IC L-VOD, the standardized $\Delta VOD_{year}$ aggregated from the nighttime VOD shows higher correlation coefficients than the aggregation methods from the combination of daytime and nighttime VOD (Fig. 8 a-f). For X-VOD

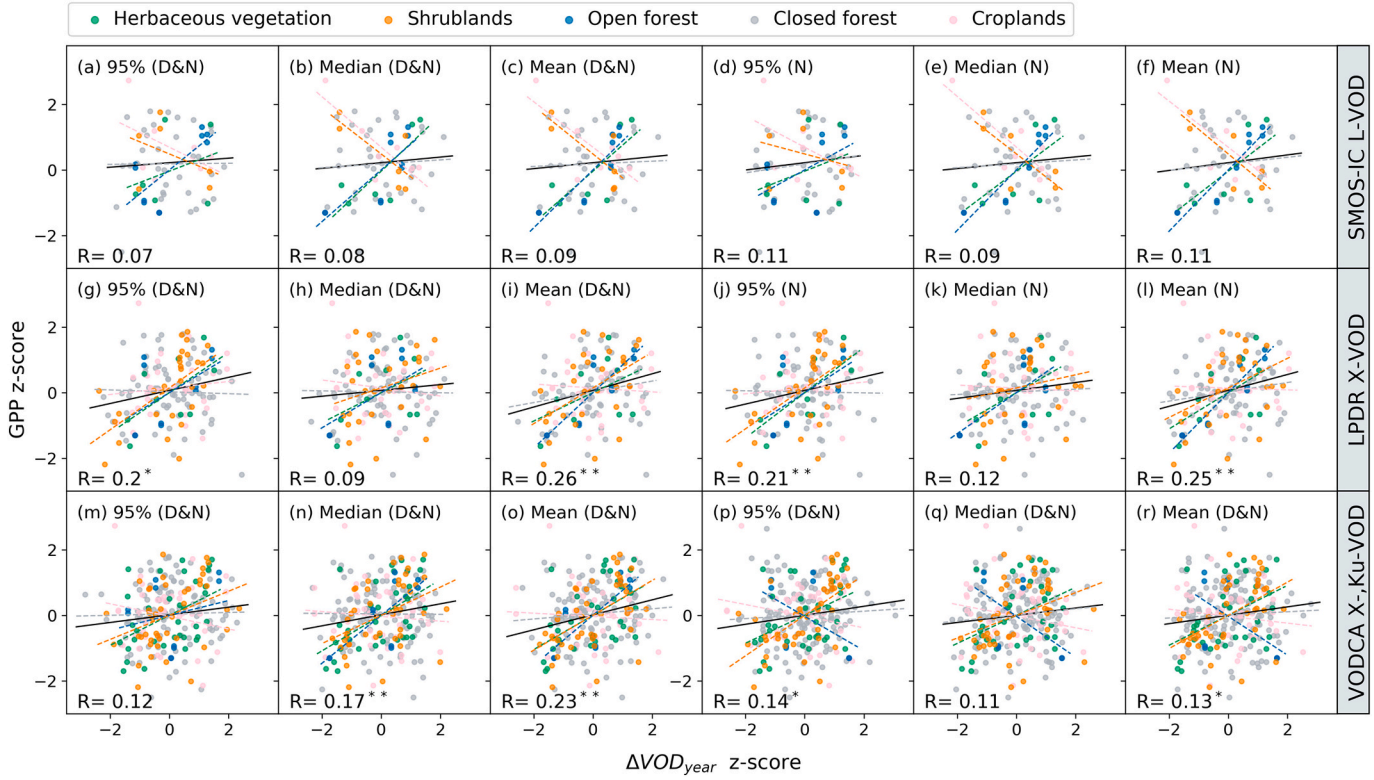


**Fig. 8.** Relationships between standardized $\Delta VOD_{year}$ and GPP annual time series from selected sites for (a-f) SMOS-IC L-VOD, (g-l) LPDR X-VOD, (m-o) VODCA X-VOD, and (p-r) VODCA Ku-VOD. "D" indicates the daytime VOD, and "N" represents the nighttime VOD. The black lines are linear regression lines for all the landcover. The colors of the scattering points and dashed regression lines indicate different landcover classes. R is the Pearson correlation coefficient. Asterisks denote significant linear correlations at 0.01 "**" and 0.05 "*" levels, respectively. Note that the number of observations available depends on the temporal overlap between flux observations and satellite data.

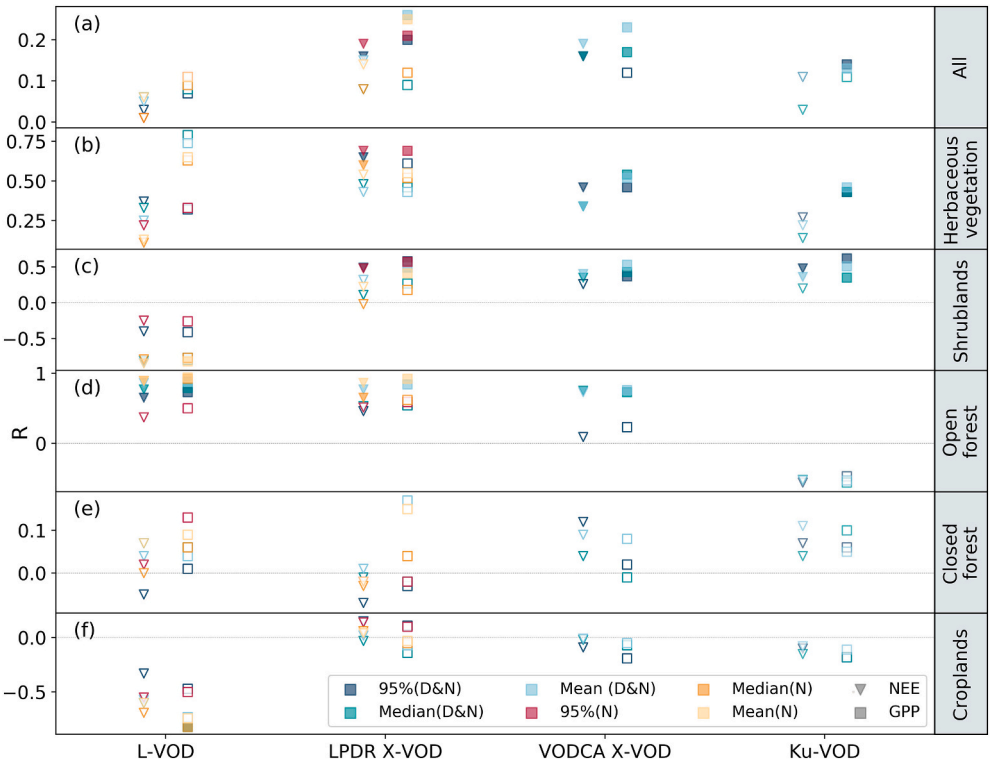


**Fig. 9.** Statistics of the Pearson correlation coefficient between standardized $\Delta VOD_{year}$ and GPP/NEE over different Copernicus land cover classes of (a) all the landcover classes, (b) herbaceous vegetation, (c) shrublands, (d) open forest, (e) closed forest and (f) croplands. "D" indicates the daytime VOD, and "N" represents the nighttime VOD. The semi-transparent symbols indicate significant relationships ($p < 0.05$) while the transparent ones indicate insignificant relationships.

derived from both LPDR and VODCA products, the standardized $\Delta VOD_{year}$ shows significant positive relationships with GPP for most of the aggregated methods (Fig. 8. g-o), and the $\Delta VOD_{year}$ from LPDR X-VOD shows stronger correlations with GPP than from VODCA X-VOD.

$\Delta VOD_{year}$ retrieved from LPDR X-VOD shows positive relationships with GPP at $p < 0.05$ level when the annual LPDR X-VOD is aggregated from the mean and 95% percentile of the nighttime or the combination of daytime and nighttime VOD (Fig. 8g-l). VODCA X-band $\Delta VOD_{year}$ is positively correlated with GPP at $p < 0.01$ level when annual VODCA X-VOD is aggregated from the median and mean of the combination of daytime and nighttime VOD (Fig. 8m-o). VODCA Ku-band $\Delta VOD_{year}$ positively correlated with GPP at $p < 0.05$ level when it is aggregated from the mean and 95% percentile of the combination of daytime and nighttime VOD (Fig. 8m-o). Insignificant positive relationships were observed for SMOS-IC L-VOD for all the annual VOD aggregation methods examined (Fig. 8a-f).

NEE is the direct measurement made by eddy covariance instruments, with positive values denoting net $CO_2$ release into the atmosphere (carbon source) and negative values denoting a flux into the land (carbon sink). Annual sums of NEE fluxes can indicate net changes in carbon stocks, including aboveground and belowground vegetation layers and the soil organic carbon pools. Interannual carbon variations in the belowground component are usually more stable than those in the aboveground vegetation layer (Carey et al., 2016; Reich et al., 2018; Tang et al., 2005). Thus, NEE may also be used for the assessment of interannual biomass carbon dynamics using VOD in the same way as GPP (Fig. S6).

The correlation coefficients between standardized $\Delta VOD_{year}$ and GPP are generally higher than those for standardized $\Delta VOD_{year}$ and NEE (Figs. 8-9, Fig. S6), particularly regarding all selected sites and all years together (Fig. 9). When looking into individual land cover types, the correlation coefficients between standardized $\Delta VOD_{year}$ and GPP are improved in comparison to those obtained with NEE for herbaceous vegetation, shrublands, and open forests (Fig. 9b-d), but they decreased or even turned into negative relationships for closed forests and croplands (Fig. 9e-f).

The correlations between standardized $\Delta VOD_{year}$ and GPP/NEE over different Copernicus landcover classes vary across classes (Fig. 9). There is a general tendency that standardized $\Delta VOD_{year}$ of X-VOD and Ku-VOD are more correlated with GPP/NEE than L-VOD for herbaceous vegetation and shrubs-dominated sites, indicating that VOD from high-frequency observations is more sensitive to GPP/NEE for short vegetation, consistent with their lower penetration depth. A similar level of significant correlation is also seen for L-VOD and X-VOD for open forests.

## 5. Discussion

In this study, we designed an approach to assess the reliability of using VOD data for estimating decadal biomass carbon dynamics across the globe, which was done by using the VWC-driven mean diurnal VOD changes as a threshold. With this method, we detected regions where dry biomass change can play a role in the decadal VOD changes, but it is noted that the respective contributions of water stress and dry biomass cannot be completely disentangled. Our results suggest a high reliability of using SMOS-IC L-VOD and LPDR X-VOD for monitoring biomass carbon dynamics over a majority of the global vegetated land surface (77% and 70%, respectively) given the use of an appropriate aggregation method to generate annual VOD (Figs. 5 and 6). In the regions with sparse vegetation (e.g. shrublands in Australia, southern Africa, and Africa Sahal), LPDR X-VOD showed a higher percentage of high-reliability pixels than L-VOD, which confirms the results from Li et al. (2021).

The relationships between interannual VOD variations and changes in water stress and biomass have been examined by comparing temporal VOD anomalies with anomalies in a newly developed biomass product obtained from optical and L-band radar data (Xu et al., 2021a) and ERA5 soil moisture data (Konings et al., 2021a). They found a spatial

consistency between averaged VOD with the biomass product similar to previous studies (Brandt et al., 2018; Fan et al., 2019; Qin et al., 2021). Yet, the correlation of temporal anomalies between VOD and the biomass product or the soil moisture product showed a complex pattern at regional scale, which indicates a dominant effect of biomass for some regions and soil moisture for others (Konings et al., 2021a). Our study revealed the spatial distributions of VOD reliabilities at pixel level globally. Our results support their conclusion by obtaining inconclusive pixels for areas with dense vegetation cover such as the tropical rainforests (Figs. 5-7), but also discrepancies are seen, such as in Australian savannas, where we obtained a high reliability in using both SMOS-IC L-VOD and LPDR X-VOD for estimating carbon temporal dynamics (Figs. 5-6). For regions labeled as inconclusive, cautious interpretation should be made when using annual VOD to study biomass dynamics in these regions, where the VOD biomass signal may be obscured by greater background noise contributed by plant water variations. However, it is important to note that results obtained from VOD in previous studies may still be valid in regions labeled as inconclusive, but the biomass signal may be weaker, making it more difficult to distinguish the effects of changes in biomass and changes in vegetation water content.

Our study shows large variations in the results using different temporal aggregation methods to obtain annual VOD. The annual VOD aggregated from the 95% percentile value of the daily observations is more sensitive to interannual carbon dynamics than using other approaches (Figs. 5-7), confirming the hypothesis made by Qin et al. (2021) that the 95% percentile of the daily VOD could minimize the annual changes in the dielectric properties of vegetation. Similarly, nighttime VOD is less sensitive to water stress than daytime VOD, and thus better for biomass carbon estimation (Frappart et al., 2020). Our results verify this well-accepted assumption given that a larger proportion of pixels is labeled as high-reliability using only nighttime observations as compared to using combined nighttime and daytime observations (Figs. 5-6). However, in regions strongly affected by ever-changing RFI, such as China, the Arabian Peninsula, and the Canada-USA border (Wigneron et al., 2021), caution should be taken when using $\Delta LVOD_{decade}$ aggregated from nighttime L-VOD to interpret decade biomass carbon dynamics, even though the pixels were labeled as 'high-reliability'. For example at the Canada-USA border, the annual L-VOD aggregated from nighttime L-VOD showed the lowest values in 2011 due to an RFI event occurring (Al-Yaari et al., 2020), further leading to a larger $\Delta LVOD_{decade}$ than the surroundings (Supplementary Fig. S3), while these pixels were still labeled as having 'high-reliability', despite this issue (Fig. 5).

Being sensitive to plant water content, VOD has been recognized as a promising tool for studying ecosystem-scale plant hydraulics (Konings et al., 2019). As a pioneer study, Konings and Gentine (2017) mapped the global degree of isohydricity (i.e. the plant stomata behaviors under water stress) using LPDR X-VOD. They assumed that plants were fully rehydrated at midnight (1:30 AM) and highly stressed at midday (1:30 PM) and obtained the isohydricity parameter by calculating the linear regression slope between the daytime and nighttime VOD observations. In this study, we used the daytime and nighttime VOD under the same assumption, but we calculated their difference to represent the diurnal water deficit. The significant correlation obtained between VOD diurnal difference and transpiration confirmed the feasibility of this assumption, whereas three aspects are worthy of further discussion as follows.

1) LPDR X-VOD shows higher correlation coefficients with transpiration than SMOS-IC L-VOD (Fig. 4). This may be due to the higher sensitivity of X-VOD to leaf components as compared to L-VOD. The GLEAM transpiration product (Martens et al., 2016) used for comparison in this study has incorporated VOD data (Liu et al., 2011; van der Schalie et al., 2015) as one of the inputs for modeling transpiration, partly determining its seasonal trends and thus impacting the correlation with VOD. Yet, the VOD diurnal difference used here would largely reduce the impacts of seasonal trends driven by leaf biomass variations.
2) Higher daytime VOD than nighttime VOD (Fig. S5). Surprisingly large areas are showing higher daytime VOD than nighttime VOD for both SMOS-IC L-VOD and LPDR X-VOD, but the spatial distribution of these areas is different, with L-VOD showing this characteristic in northern and eastern Europe, Africa, southeast Asia, western Australia, and western South America and X-VOD in the arctic regions at latitudes higher than 50 N°. Currently, this is poorly understood and the reasons behind can be complex. First, data uncertainties and artifacts may be one possible reason. For the descending mode (daytime 6:00 PM) of SMOS, the antennas are oriented towards the south, where there is lower RFI, leading to higher SMOS-IC L-VOD values (Oliva et al., 2016). But this effect should be relatively low in South and North America, for which areas we still see higher daytime L-VOD than nighttime L-VOD, suggesting that data uncertainties and artifacts may not be the only reason. Second, with two satellite overpassing times, the VODs may not be fully able to capture the short-term plant water variations. Moreover, dew formation and diurnal variations in rainfall may also play a role (Xu et al., 2021b). However, as we used 8-day composites to calculate the VOD diurnal difference, many of the impacts mentioned above should be minimized and the significant correlation with transpiration indeed suggests that the VOD diurnal difference represents the diurnal plant water cycle.
3) To fill the data gaps in the original satellite observations, we used an 8-day composite of daytime and nighttime observations of VOD. This may lead to decreased dynamics of $\Delta VOD_{day}$ in comparison to the actual dynamics in VWC, particularly in regions covered by short vegetation (e.g. savannas, shrublands, grasslands), in which VWC shows noticeable changes over short periods (Chan et al., 2013). However, considering that we used the averaged $\Delta VOD_{day}$ over multiple years for the comparison with the VOD decadal variations, the impacts of using 8-day temporal composites of VOD should be minimal, and the moderate and strong correlations between 8-day composites of $\Delta VOD_{day}$ and transpiration for SMOS-IC L-VOD and LPDR X-VOD, respectively suggest it to be a strong proxy for diurnal changes in VWC.

The high consistency between VOD and biomass carbon over space has been widely documented, although different microwave frequencies, algorithms, and VOD products showed varying performances (Li et al., 2021). Yet, the temporal relationship between VOD and biomass carbon has been rarely examined due to the lack of global long-term biomass data. In this study, we used GPP and NEE data from appropriate flux sites across the globe to evaluate the reliability of three VOD products for the estimation of interannual biomass carbon dynamics. The positive correlations between standardized $\Delta VOD_{year}$ and GPP (NEE) suggest that VOD does contain information on interannual carbon dynamics over the footprints of the eddy covariance flux towers, but there are large uncertainties in the analysis as indicated by the modest correlation coefficients obtained.

For the comparison with VOD, the ideal field measurements would be the net carbon changes in the aboveground vegetation layer instead of GPP or NEE. NEE is the net carbon exchange of the whole ecosystem, including the above and below-ground carbon pool. The fraction of global belowground biomass varies with plant species (Mokany et al., 2006) and the biomass allocation to roots could vary with local environmental conditions and plant species (Ribeiro et al., 2011). For example, studies documented that 22% of biomass was allocated to roots for forests (Ma et al., 2021), 67% for grassland (Ma et al., 2021), and 47% for shrubs (Müller et al., 2000). GPP is the gross carbon uptake by the vegetation layer, it eliminates the contribution from soil respiration to the observed NEE, and approximately 50% of the GPP is generally considered as the net carbon sequestrated by the ecosystem (Waring et al., 2016), making the relationships between standardized $\Delta VOD_{year}$

and GPP stronger than NEE, while in croplands and closed forests, disturbance such as crop management and deforestation within the tested VOD pixels varies with pixels introduces uncertainties in the relationship between $\Delta VOD_{year}$ and GPP/NEE, and making the relationships insignificant (Fig. 9).

Considering the above-mentioned uncertainties also in the context of the large spatial mismatch in the point-to-pixel comparison, it is unlikely that very high correlations would be achievable from this analysis. However, the higher correlation coefficients with GPP than with NEE indicate that we do increase the relationship between eddy covariance measurement and $\Delta VOD_{year}$ by removing temporal variations in the soil respiration component, suggesting the validity of the method used in the study. Overall, the positive correlation between eddy covariance measurements and $\Delta VOD_{year}$ does support the use of VOD for estimating carbon dynamics at the interannual scale. It should be noted that the correlations between $\Delta VOD_{year}$ and GPP/NEE are generally less significant for L-VOD than for X-VOD (Figs. 8-9, Fig. S6), which is partly because fewer paired $\Delta VOD_{year}$ and GPP/NEE data are available due to the shorter period of the SMOS-IC observations.

## 6. Conclusions

In this paper, we introduced a new method to evaluate the reliability of VOD to estimate the interannual carbon dynamics. SMOS-IC L-VOD and LPDR X-VOD were used to estimate plant water buffering and annual plant water status based on the assumption that the VOD diurnal variation can be a good proxy for the degree of plant water deficit during daytime. We found that X-VOD is clearly better than L-VOD in capturing the plant water deficit caused by transpiration, due to the higher sensitivity of the X-band frequency to leaf water content. Through the comparison between VOD interannual and diurnal variations, the pixels of high reliability or inconclusive in estimating the interannual biomass dynamics were mapped for both L-VOD and LPDR X-VOD data. L-VOD was found to be more sensitive to biomass dynamics signals than X-VOD for all land cover types across the globe, except for shrublands regions. From our analyses, we can conclude that the annual VOD aggregated from the 95% percentile of the nighttime VOD captures interannual biomass change with higher reliability regardless of the frequency of the satellite product, and we recommend this way of aggregating VOD from daily to annual observations for monitoring biomass dynamics at regional to global scale. GPP/NEE data measured at flux sites of homogeneous land cover was used as a measured evaluation of interannual VOD-based carbon estimations. The positive relationship between VOD difference between successive years and GPP/NEE indicates that VOD can capture interannual carbon dynamics signals over ecosystem scales and the capability of VOD to estimate carbon differs among microwave frequencies and products. Our results show the ecological significance of satellite microwave VOD retrievals for monitoring biomass carbon dynamics, and also indicate the potential utility of using multi-frequency VOD retrievals to estimate decadal and interannual carbon dynamics over different ecosystems. Moreover, the next-generation microwave sensors like Copernicus Imaging Microwave Radiometer (CIMR) have the capability for simultaneous multi-frequency TB retrievals, which will allow for multi-frequency VOD retrievals with consistent space/time sampling and may have higher reliability for estimating carbon dynamics.

## Authors contribution

**Yujie Dou:** Methodology, Data curation, Formal analysis, Writing -original draft, Writing- reviewing and editing. **Feng Tian:** Conceptualization, Methodology, Writing - original draft, Writing- reviewing and editing, Funding acquisition, Supervision. **Jean-Pierre Wigneron:** Resources, Writing- reviewing and editing. **Torbern Tagesson:** Writing-reviewing and editing. **Jinyang Du:** Resources, Writing- reviewing and editing. **Martin Brandt:** Writing- reviewing and editing. **Yi Liu:** Writing- reviewing and editing. **Linqing Zou:** Writing- reviewing and editing. **John S Kimball:** Resources, Writing- reviewing and editing. **Rasmus Fensholt:** Writing- reviewing and editing.

## Declaration of Competing Interest

The authors declare that they have no known competing financial interests or personal relationships that could have appeared to influence the work reported in this paper.

## Data availability

Data will be made available on request.

## Acknowledgments

This work is supported by the Nation Natural Science Foundation of China (Grant No. 42001299) and the Seed Fund Program for Sino-Foreign Joint Scientific Research Platform of Wuhan University (No. WHUZZJJ202205). Torbern Tagesson is funded by the Swedish National Space Agency (SNSA Dnr: 2021-00144 and 2021-00111), and Formas (Dnr: 2021-00644).

## Appendix A. Supplementary data

Supplementary data to this article can be found online at https://doi.org/10.1016/j.rse.2022.113390.

## References

Al-Yaari, A., Wigneron, J., Ciais, P., Reichstein, M., Ballantyne, A., Ogée, J., Ducharne, A., Swenson, J.J., Frappart, F., Fan, L., Wingate, L., Li, X., Hufkens, K., Knapp, A.K., 2020. Asymmetric responses of ecosystem productivity to rainfall anomalies vary inversely with mean annual rainfall over the conterminous United States. Glob. Change Biol. 26, 6959–6973. https://doi.org/10.1111/gcb.15345.

Baccini, A., Goetz, S.J., Walker, W.S., Laporte, N.T., Sun, M., Sulla-Menashe, D., Hackler, J., Beck, P.S.A., Dubayah, R., Friedl, M.A., Samanta, S., Houghton, R.A., 2012. Estimated carbon dioxide emissions from tropical deforestation improved by carbon-density maps. Nat. Clim. Change 2, 182–185. https://doi.org/10.1038/nclimate1354.

Brandt, M., Wigneron, J.-P., Chave, J., Tagesson, T., Penuelas, J., Ciais, P., Rasmussen, K., Tian, F., Mbow, C., Al-Yaari, A., Rodriguez-Fernandez, N., Schurgers, G., Zhang, W., Chang, J., Kerr, Y., Verger, A., Tucker, C., Mialon, A., Rasmussen, L.V., Fan, L., Fensholt, R., 2018. Satellite passive microwaves reveal recent climate-induced carbon losses in African drylands. Nat. Ecol. Evol. 2, 827–835. https://doi.org/10.1038/s41559-018-0530-6.

Buchhorn, M., Lesiv, M., Tsendbazar, N.-E., Herold, M., Bertels, L., Smets, B., 2020. Copernicus global land cover layers—collection2. Remote Sens. 12, 1044. https://doi.org/10.3390/rs12061044.

Carey, J.C., Tang, J., Templer, P.H., Kroeger, K.D., Crowther, T.W., Burton, A.J., Dukes, J.S., Emmett, B., Frey, S.D., Heskel, M.A., Jiang, L., Machmuller, M.B., Mohan, J., Panetta, A.M., Reich, P.B., Reinsch, S., Wang, X., Allison, S.D., Bamminger, C., Bridgham, S., Collins, S.L., de Dato, G., Eddy, W.C., Enquist, B.J., Estiarte, M., Harte, J., Henderson, A., Johnson, B.R., Larsen, K.S., Luo, Y., Marhan, S., Melillo, J.M., Peñuelas, J., Pfeifer-Meister, L., Poll, C., Rastetter, E., Reinmann, A.B., Reynolds, L.L., Schmidt, I.K., Shaver, G.R., Strong, A.L., Suseela, V., Tietema, A., 2016. Temperature response of soil respiration largely unaltered with experimental warming. Proc. Natl. Acad. Sci. U. S. A. 113, 13797–13802. https://doi.org/10.1073/pnas.1605365113.

Chan, S., Bindlish, R., Hunt, R., Jackson, T., Kimball, J., 2013. Vegetation Water Content. Jet Propulsion Laboratory, California Institute of Technology, Pasadena, CA, USA 18.

Chaparro, D., Duveiller, G., Piles, M., Cescatti, A., Vall-llossera, M., Camps, A., Entekhabi, D., 2019. Sensitivity of L-band vegetation optical depth to carbon stocks in tropical forests: a comparison to higher frequencies and optical indices. Remote Sens. Environ. 232, 111303 https://doi.org/10.1016/j.rse.2019.111303.

Cui, Q., Shi, J., Du, J., Zhao, T., Xiong, C., 2015. An approach for monitoring global vegetation based on multiangular observations from SMOS. IEEE JSel. Top. Appl. Earth Observations Remote Sensing 8, 604–616. https://doi.org/10.1109/JSTARS.2015.2388698.

Daly, E., Porporato, A., Rodriguez-Iturbe, I., 2004. Coupled dynamics of photosynthesis, transpiration, and soil water balance. Part I: upscaling from hourly to daily level. J. Hydrometeor 5, 546–558. https://doi.org/10.1175/1525-7541(2004)005<0546:CDOPTA>2.0.CO;2.

Dawson, T.E., Burgess, S.S.O., Tu, K.P., Oliveira, R.S., Santiago, L.S., Fisher, J.B., Simonin, K.A., Ambrose, A.R., 2007. Nighttime transpiration in woody plants from contrasting ecosystems. Tree Physiol. 27, 561–575. https://doi.org/10.1093/treephys/27.4.561.

Didan, Kamel, 2015. MOD13C2 MODIS/Terra Vegetation Indices Monthly L3 Global 0.05Deg CMG V006. https://doi.org/10.5067/MODIS/MOD13C2.006.

Du, J., Kimball, J.S., Jones, L.A., Kim, Y., Glassy, J., Watts, J.D., 2017. A global satellite environmental data record derived from AMSR-E and AMSR2 microwave earth observations. Earth Syst. Sci. Data 9, 791–808. https://doi.org/10.5194/essd-9-791-2017.

Dubayah, R., Blair, J.B., Goetz, S., Fatoyinbo, L., Hansen, M., Healey, S., Hofton, M., Hurtt, G., Kellner, J., Luthcke, S., Armston, J., Tang, H., Duncanson, L., Hancock, S., Jantz, P., Marselis, S., Patterson, P.L., Qi, W., Silva, C., 2020. The global ecosystem dynamics investigation: high-resolution laser ranging of the Earth's forests and topography. Sci. Remote Sens. 1, 100002 https://doi.org/10.1016/j.srs.2020.100002.

Duncanson, L., Kellner, J.R., Armston, J., Dubayah, R., Minor, D.M., Hancock, S., Healey, S.P., Patterson, P.L., Saarela, S., Marselis, S., Silva, C.E., Bruening, J., Goetz, S.J., Tang, H., Hofton, M., Blair, B., Luthcke, S., Fatoyinbo, L., Abernethy, K., Alonso, A., Andersen, H.-E., Aplin, P., Baker, T.R., Barbier, N., Bastin, J.F., Biber, P., Boeckx, P., Bogaert, J., Boschetti, L., Boucher, P.B., Boyd, D.S., Burslem, D.F.R.P., Calvo-Rodriguez, S., Chave, J., Chazdon, R.L., Clark, D.B., Clark, D.A., Cohen, W.B., Coomes, D.A., Corona, P., Cushman, K.C., Cutler, M.E.J., Dalling, J.W., Dalponte, M., Dash, J., Deng, S., Ellis, P.W., Erasmus, B., Fekety, P.A., Fernandez-Landa, A., Ferraz, A., Fischer, R., Fisher, A.G., García-Abril, A., Gobakken, T., Hacker, J.M., Heurich, M., Hill, R.A., Hopkinson, C., Huang, H., Hubbell, S.P., Hudak, A.T., Huth, A., Imbach, B., Jeffery, K.J., Katoh, M., Kearsley, E., Kenfack, D., Kljun, N., Knapp, N., Král, K., Krůček, M., Labrière, N., Lewis, S.L., Longo, M., Lucas, R.M., De-Miguel, S., Main, R., Manzanera, J.A., Martínez, R.V., Mathieu, R., Memiaghe, H., Meyer, V., Mendoza, A.M., Monerris, A., Montesano, P., Morsdorf, F., Næsset, E., Naidoo, L., Nilus, R., O'Brien, M., Orwig, D.A., Papathanassiou, K., Parker, G., Philipson, C., Phillips, O.L., Pisek, J., Poulsen, J.R., Pretzsch, H., Rüdiger, C., Saatchi, S., Sanchez-Azofeifa, A., Sanchez-Lopez, N., Scholes, R., Silva, C.A., Simard, M., Skidmore, A., Stereńczak, K., Tanase, M., Torresan, C., Valbuena, R., Verbeeck, H., Vrska, T., Wessels, K., White, J.C., White, L.J.T., Zahabu, E., Zgraggen, C., 2022. Aboveground biomass density models for NASA's Global Ecosystem Dynamics Investigation (GEDI) lidar mission. Remote Sens. Environ. 270, 112845. https://doi.org/10.1016/j.rse.2021.112845.

Fan, L., Wigneron, J.-P., Ciais, P., Chave, J., Brandt, M., Fensholt, R., Saatchi, S.S., Bastos, A., Al-Yaari, A., Hufkens, K., Qin, Y., Xiao, X., Chen, C., Myneni, R.B., Fernandez-Moran, R., Mialon, A., Rodriguez-Fernandez, N.J., Kerr, Y., Tian, F., Peñuelas, J., 2019. Satellite-observed pantropical carbon dynamics. Nat. Plants 5, 944–951. https://doi.org/10.1038/s41477-019-0478-9.

Fernandez-Moran, R., Al-Yaari, A., Mialon, A., Mahmoodi, A., Al Bitar, A., De Lannoy, G., Rodriguez-Fernandez, N., Lopez-Baeza, E., Kerr, Y., Wigneron, J.-P., 2017. SMOS-IC: an alternative SMOS soil moisture and vegetation optical depth product. Remote Sens. 9, 457. https://doi.org/10.3390/rs9050457.

Frappart, F., Wigneron, J.-P., Li, X., Liu, X., Al-Yaari, A., Fan, L., Wang, M., Moisy, C., Le Masson, E., Aoulad Lafkih, Z., Vallé, C., Ygorra, B., Baghdadi, N., 2020. Global monitoring of the vegetation dynamics from the vegetation optical depth (VOD): a review. Remote Sens. 12, 2915. https://doi.org/10.3390/rs12182915.

Friedl, Mark, Gray, Josh, Sulla-Menashe, Damien, 2019. MCD12Q2 MODIS/Terra+Aqua Land Cover Dynamics Yearly L3 Global 500m SIN Grid V006. https://doi.org/10.5067/MODIS/MCD12Q2.006.

Friedlingstein, P., O'Sullivan, M., Jones, M.W., Andrew, R.M., Hauck, J., Olsen, A., Peters, G.P., Peters, W., Pongratz, J., Sitch, S., Le Quéré, C., Canadell, J.G., Ciais, P., Jackson, R.B., Alin, S., Aragão, L.E.O.C., Arneth, A., Arora, V., Bates, N.R., Becker, M., Benoit-Cattin, A., Bittig, H.C., Bopp, L., Bultan, S., Chandra, N., Chevallier, F., Chini, L.P., Evans, W., Florentie, L., Forster, P.M., Gasser, T., Gehlen, M., Gilfillan, D., Gkritzalis, T., Gregor, L., Gruber, N., Harris, I., Hartung, K., Haverd, V., Houghton, R.A., Ilyina, T., Jain, A.K., Joetzjer, E., Kadono, K., Kato, E., Kitidis, V., Korsbakken, J.I., Landschützer, P., Lefèvre, N., Lenton, A., Lienert, S., Liu, Z., Lombardozzi, D., Marland, G., Metzl, N., Munro, D.R., Nabel, J.E.M.S., Nakaoka, S.-I., Niwa, Y., O'Brien, K., Ono, T., Palmer, P.I., Pierrot, D., Poulter, B., Resplandy, L., Robertson, E., Rödenbeck, C., Schwinger, J., Séférian, R., Skjelvan, I., Smith, A.J.P., Sutton, A.J., Tanhua, T., Tans, P.P., Tian, H., Tilbrook, B., van der Werf, G., Vuichard, N., Walker, A.P., Wanninkhof, R., Watson, A.J., Willis, D., Wiltshire, A.J., Yuan, W., Yue, X., Zaehle, S., 2020. Global carbon budget 2020. Earth Syst. Sci. Data 12, 3269–3340. https://doi.org/10.5194/essd-12-3269-2020.

Holtzman, N.M., Anderegg, L.D.L., Kraatz, S., Mavrovic, A., Sonnentag, O., Pappas, C., Cosh, M.H., Langlois, A., Lakhankar, T., Tesser, D., Steiner, N., Colliander, A., Roy, A., Konings, A.G., 2021. L-band vegetation optical depth as an indicator of plant water potential in a temperate deciduous forest stand. Biogeosciences 18, 739–753. https://doi.org/10.5194/bg-18-739-2021.

Konings, A.G., Gentine, P., 2017. Global variations in ecosystem-scale isohydricity. Glob Change Biol 23, 891–905. https://doi.org/10.1111/gcb.13389.

Konings, A.G., Holtzman, N.M., Rao, K., Xu, L., Saatchi, S.S., 2021a. Interannual variations of vegetation optical depth are due to both water stress and biomass changes. Geophys. Res. Lett. 48 https://doi.org/10.1029/2021GL095267.

Konings, A.G., Rao, K., Steele-Dunne, S.C., 2019. Macro to micro: microwave remote sensing of plant water content for physiology and ecology. New Phytol 223, 1166–1172. https://doi.org/10.1111/nph.15808.

Konings, A.G., Saatchi, S.S., Frankenberg, C., Keller, M., Leshyk, V., Anderegg, W.R.L., Humphrey, V., Matheny, A.M., Trugman, A., Sack, L., Agee, E., Barnes, M.L., Binks, O., Cawse-Nicholson, K., Christoffersen, B.O., Entekhabi, D., Gentine, P., Holtzman, N.M., Katul, G.G., Liu, Y., Longo, M., Martinez-Vilalta, J., McDowell, N., Meir, P., Mencuccini, M., Mrad, A., Novick, K.A., Oliveira, R.S., Siqueira, P., Steele-Dunne, S.C., Thompson, D.R., Wang, Y., Wehr, R., Wood, J.D., Xu, X., Zuidema, P.A., 2021. Detecting forest response to droughts with global observations of vegetation water content. Glob. Change Biol gcb. 15872 https://doi.org/10.1111/gcb.15872.

Konings, A.G., Yu, Y., Xu, L., Yang, Y., Schimel, D.S., Saatchi, S.S., 2017. Active microwave observations of diurnal and seasonal variations of canopy water content across the humid African tropical forests. Geophys. Res. Lett. 44, 2290–2299. https://doi.org/10.1002/2016GL072388.

Lang, N., Kalischek, N., Armston, J., Schindler, K., Dubayah, R., Wegner, J.D., 2022. Global canopy height regression and uncertainty estimation from GEDI LIDAR waveforms with deep ensembles. Remote Sens. Environ. 268, 112760 https://doi.org/10.1016/j.rse.2021.112760.

Li, X., Wigneron, J.-P., Frappart, F., Fan, L., Ciais, P., Fensholt, R., Entekhabi, D., Brandt, M., Konings, A.G., Liu, X., Wang, M., Al-Yaari, A., Moisy, C., 2021. Global-scale assessment and inter-comparison of recently developed/reprocessed microwave satellite vegetation optical depth products. Remote Sens. Environ. 253, 112208 https://doi.org/10.1016/j.rse.2020.112208.

Taiz, Lincoln, 2014. Plant Physiology and Development. In: Sixth edition. Sinauer Associates, Inc. p, p. 65.

Liu, Y.Y., de Jeu, R.A.M., McCabe, M.F., Evans, J.P., van Dijk, A.I.J.M., 2011. Global long-term passive microwave satellite-based retrievals of vegetation optical depth. Geophys. Res. Lett. 38, n/a-n/a. https://doi.org/10.1029/2011GL048684.

Liu, Y.Y., van Dijk, A.I.J.M., de Jeu, R.A.M., Canadell, J.G., McCabe, M.F., Evans, J.P., Wang, G., 2015. Recent reversal in loss of global terrestrial biomass. Nat. Clim. Change 5, 470–474. https://doi.org/10.1038/nclimate2581.

Ma, H., Mo, L., Crowther, T.W., Maynard, D.S., van den Hoogen, J., Stocker, B.D., Terrer, C., Zohner, C.M., 2021. The global distribution and environmental drivers of aboveground versus belowground plant biomass. Nat. Ecol. Evol. https://doi.org/10.1038/s41559-021-01485-1.

Martens, B., Miralles, D.G., Lievens, H., van der Schalie, R., de Jeu, R.A.M., Férnandez-Prieto, D., Beck, H.E., Dorigo, W.A., Verhoest, N.E.C., 2016. GLEAM v3: satellite-based land evaporation and root-zone soil moisture (preprint). Hydrology. https://doi.org/10.5194/gmd-2016-162.

Meinzer, F.C., Johnson, D.M., Lachenbruch, B., McCulloh, K.A., Woodruff, D.R., 2009. Xylem hydraulic safety margins in woody plants: coordination of stomatal control of xylem tension with hydraulic capacitance. Funct. Ecol. 23, 922–930. https://doi.org/10.1111/j.1365-2435.2009.01577.x.

Miralles, D.G., Holmes, T.R.H., De Jeu, R.A.M., Gash, J.H., Meesters, A.G.C.A., Dolman, A.J., 2011. Global land-surface evaporation estimated from satellite-based observations. Hydrol. Earth Syst. Sci. 15, 453–469. https://doi.org/10.5194/hess-15-453-2011.

Moesinger, L., Dorigo, W., de Jeu, R., van der Schalie, R., Scanlon, T., Teubner, I., Forkel, M., 2020. The global long-term microwave vegetation optical depth climate archive (VODCA). Earth Syst. Sci. Data 12, 177–196. https://doi.org/10.5194/essd-12-177-2020.

Mokany, K., Raison, R.J., Prokushkin, A.S., 2006. Critical analysis of root : shoot ratios in terrestrial biomes: ROOT : SHOOT RATIOS IN TERRESTRIAL BIOMES. Glob. Chang. Biol. 12, 84–96. https://doi.org/10.1111/j.1365-2486.2005.001043.x.

Momen, M., Wood, J.D., Novick, K.A., Pangle, R., Pockman, W.T., McDowell, N.G., Konings, A.G., 2017. Interacting effects of leaf water potential and biomass on vegetation optical depth: effects of LWP and biomass on VOD. J. Geophys. Res. Biogeosci. 122, 3031–3046. https://doi.org/10.1002/2017JG004145.

Moncrieff, J.B., Malhi, Y., Leuning, R., 1996. The propagation of errors in long-term measurements of land-atmosphere fluxes of carbon and water. Glob. Chang. Biol. 2, 231–240. https://doi.org/10.1111/j.1365-2486.1996.tb00075.x.

Müller, I., Schmid, B., Weiner, J., 2000. The effect of nutrient availability on biomass allocation patterns in 27 species of herbaceous plants. Perspect. Plant Ecol. Evol. System. 3, 115–127. https://doi.org/10.1078/1433-8319-00007.

Ni-Meister, W., Rojas, A., Lee, S., 2022. Direct use of large-footprint lidar waveforms to estimate aboveground biomass. Remote Sens. Environ. 280, 113147 https://doi.org/10.1016/j.rse.2022.113147.

Njoku, E.G., Ashcroft, P., Chan, T.K., Li, Li, 2005. Global survey and statistics of radio-frequency interference in AMSR-E land observations. IEEE Trans. Geosci. Remote Sensing 43, 938–947. https://doi.org/10.1109/TGRS.2004.837507.

Oliva, R., Daganzo, E., Richaume, P., Kerr, Y., Cabot, F., Soldo, Y., Anterrieu, E., Reul, N., Gutierrez, A., Barbosa, J., Lopes, G., 2016. Status of radio frequency interference (RFI) in the 1400–1427 MHz passive band based on six years of SMOS mission. Remote Sens. Environ. 180, 64–75. https://doi.org/10.1016/j.rse.2016.01.013.

Pastorello, G., Hörtnagl, L., 2020. The FLUXNET2015 dataset and the ONEFlux processing pipeline for eddy covariance data. Scientific Data 7, 225. https://doi.org/10.1038/s41597-020-0534-3.

Piao, S., Wang, X., Wang, K., Li, X., Bastos, A., Canadell, J.G., Ciais, P., Friedlingstein, P., Sitch, S., 2020. Interannual variation of terrestrial carbon cycle: issues and perspectives. Glob. Change Biol. 26, 300–318. https://doi.org/10.1111/gcb.14884.

Qin, Y., Xiao, X., Wigneron, J.-P., Ciais, P., Brandt, M., Fan, L., Li, X., Crowell, S., Wu, X., Doughty, R., Zhang, Y., Liu, F., Sitch, S., Moore, B., 2021. Carbon loss from forest degradation exceeds that from deforestation in the Brazilian Amazon. Nat. Clim. Chang. 11, 442–448. https://doi.org/10.1038/s41558-021-01026-5.

Rao, K., Anderegg, W.R.L., Sala, A., Martínez-Vilalta, J., Konings, A.G., 2019. Satellite-based vegetation optical depth as an indicator of drought-driven tree mortality. Remote Sens. Environ. 227, 125–136. https://doi.org/10.1016/j.rse.2019.03.026.

Reich, P.B., Sendall, K.M., Stefanski, A., Rich, R.L., Hobbie, S.E., Montgomery, R.A., 2018. Effects of climate warming on photosynthesis in boreal tree species depend on soil moisture. Nature 562, 263–267. https://doi.org/10.1038/s41586-018-0582-4.

Ribeiro, S.C., Fehrmann, L., Soares, C.P.B., Jacovine, L.A.G., Kleinn, C., de Oliveira Gaspar, R., 2011. Above- and belowground biomass in a Brazilian cerrado. For. Ecol. Manag. 262, 491–499. https://doi.org/10.1016/j.foreco.2011.04.017.

Rodríguez-Fernández, N.J., Mialon, A., Mermoz, S., Bouvet, A., Richaume, P., Al Bitar, A., Al-Yaari, A., Brandt, M., Kaminski, T., Le Toan, T., Kerr, Y.H., Wigneron, J.-P., 2018. An evaluation of SMOS L-band vegetation optical depth (L-VOD) data sets:

high sensitivity of L-VOD to above-ground biomass in Africa. Biogeosciences 15, 4627–4645. https://doi.org/10.5194/bg-15-4627-2018.

Saatchi, S.S., Harris, N.L., Brown, S., Lefsky, M., Mitchard, E.T.A., Salas, W., Zutta, B.R., Buermann, W., Lewis, S.L., Hagen, S., Petrova, S., White, L., Silman, M., Morel, A., 2011. Benchmark map of forest carbon stocks in tropical regions across three continents. Proc. Nat. Acad. Sci. 108, 9899–9904. https://doi.org/10.1073/pnas.1019576108.

Santi, E., Pettinato, S., Paloscia, S., Pampaloni, P., Macelloni, G., Brogioni, M., 2012. An algorithm for generating soil moisture and snow depth maps from microwave spaceborne radiometers: HydroAlgo. Hydrol. Earth Syst. Sci. 16, 3659–3676. https://doi.org/10.5194/hess-16-3659-2012.

Scholze, M., Kaminski, T., Knorr, W., Voßbeck, M., Wu, M., Ferrazzoli, P., Kerr, Y., Mialon, A., Richaume, P., Rodríguez-Fernández, N., Vittucci, C., Wigneron, J.-P., Mecklenburg, S., Drusch, M., 2019. Mean european carbon sink over 2010–2015 estimated by simultaneous assimilation of atmospheric CO 2, soil moisture, and vegetation optical depth. Geophys. Res. Lett. 46, 13796–13803. https://doi.org/10.1029/2019GL085725.

Shi, J., Jackson, T., Tao, J., Du, J., Bindlish, R., Lu, L., Chen, K., 2008. Microwave vegetation indices for short vegetation covers from satellite passive microwave sensor AMSR-E. Remote Sens. Environ. 112, 4285–4300. https://doi.org/10.1016/j.rse.2008.07.015.

Tagesson, T., Ardö, J., Guiro, I., Cropley, F., Mbow, C., Horion, S., Ehammer, A., Mougin, E., Delon, C., Galy-Lacaux, C., Fensholt, R., 2016. Very high CO 2 exchange fluxes at the peak of the rainy season in a west african grazed semi-arid savanna ecosystem. Geografisk Tidsskrift-Danish J. Geogr. 116, 93–109. https://doi.org/10.1080/00167223.2016.1178072.

Tang, J., Baldocchi, D.D., Xu, L., 2005. Tree photosynthesis modulates soil respiration on a diurnal time scale. Glob. Chang. Biol. 11, 1298–1304. https://doi.org/10.1111/j.1365-2486.2005.00978.x.

Teubner, I.E., Forkel, M., Camps-Valls, G., Jung, M., Miralles, D.G., Tramontana, G., van der Schalie, R., Vreugdenhil, M., Mösinger, L., Dorigo, W.A., 2019. A carbon sink-driven approach to estimate gross primary production from microwave satellite observations. Remote Sens. Environ. 229, 100–113. https://doi.org/10.1016/j.rse.2019.04.022.

Tian, F., Brandt, M., Liu, Y.Y., Rasmussen, K., Fensholt, R., 2017. Mapping gains and losses in woody vegetation across global tropical drylands. Glob Change Biol 23, 1748–1760. https://doi.org/10.1111/gcb.13464.

Tian, F., Brandt, M., Liu, Y.Y., Verger, A., Tagesson, T., Diouf, A.A., Rasmussen, K., Mbow, C., Wang, Y., Fensholt, R., 2016. Remote sensing of vegetation dynamics in drylands: evaluating vegetation optical depth (VOD) using AVHRR NDVI and in situ green biomass data over west African Sahel. Remote Sens. Environ. 177, 265–276. https://doi.org/10.1016/j.rse.2016.02.056.

Tian, F., Wigneron, J.-P., Ciais, P., Chave, J., Ogée, J., Peñuelas, J., Ræbild, A., Domec, J.-C., Tong, X., Brandt, M., Mialon, A., Rodriguez-Fernandez, N., Tagesson, T., Al-Yaari, A., Kerr, Y., Chen, C., Myneni, R.B., Zhang, W., Ardö, J., Fensholt, R., 2018. Coupling of ecosystem-scale plant water storage and leaf phenology observed by satellite. Nat. Ecol. Evol. 2, 1428–1435. https://doi.org/10.1038/s41559-018-0630-3.

Vaglio Laurin, G., Vittucci, C., Tramontana, G., Ferrazzoli, P., Guerriero, L., Papale, D., 2020. Monitoring tropical forests under a functional perspective with satellite-based vegetation optical depth. Glob. Change Biol. 26, 3402–3416. https://doi.org/10.1111/gcb.15072.

van der Schalie, R., Parinussa, R.M., Renzullo, L.J., van Dijk, A.I.J.M., Su, C.-H., de Jeu, R.A.M., 2015. SMOS soil moisture retrievals using the land parameter retrieval model: evaluation over the Murrumbidgee catchment, Southeast Australia. Remote Sens. Environ. 163, 70–79. https://doi.org/10.1016/j.rse.2015.03.006.

Vittucci, C., Vaglio Laurin, G., Tramontana, G., Ferrazzoli, P., Guerriero, L., Papale, D., 2019. Vegetation optical depth at L-band and above ground biomass in the tropical range: evaluating their relationships at continental and regional scales. Int. J. Appl. Earth Obs. Geoinf. 77, 151–161. https://doi.org/10.1016/j.jag.2019.01.006.

Waring, R., Landsberg, J., Linder, S., 2016. Tamm review: insights gained from light use and leaf growth efficiency indices. For. Ecol. Manag. 379, 232–242. https://doi.org/10.1016/j.foreco.2016.08.023.

Wigneron, J.-P., Fan, L., Ciais, P., Bastos, A., Brandt, M., Chave, J., Saatchi, S., Baccini, A., Fensholt, R., 2020. Tropical forests did not recover from the strong 2015–2016 El Niño event. Sci. Adv. 6, eaay4603. https://doi.org/10.1126/sciadv.aay4603.

Wigneron, J.-P., Li, X., Frappart, F., Fan, L., Al-Yaari, A., De Lannoy, G., Liu, X., Wang, M., Le Masson, E., Moisy, C., 2021. SMOS-IC data record of soil moisture and L-VOD: historical development, applications and perspectives. Remote Sens. Environ. 254, 112238 https://doi.org/10.1016/j.rse.2020.112238.

Xu, L., Saatchi, S.S., Yang, Y., Yu, Y., Pongratz, J., Bloom, A.A., Bowman, K., Worden, J., Liu, J., Yin, Y., Domke, G., McRoberts, R.E., Woodall, C., Nabuurs, G.-J., de-Miguel, S., Keller, M., Harris, N., Maxwell, S., Schimel, D., 2021. Changes in global terrestrial live biomass over the 21st century. Sci. Adv. 7 https://doi.org/10.1126/sciadv.abe9829 eabe9829.

Xu, X., Konings, A.G., Longo, M., Feldman, A., Xu, L., Saatchi, S., Wu, D., Wu, J., Moorcroft, P., 2021. Leaf surface water, not plant water stress, drives diurnal variation in tropical forest canopy water content. New Phytol. 231, 122–136. https://doi.org/10.1111/nph.17254.

Yu, Y., Saatchi, S., 2016. Sensitivity of L-band SAR backscatter to aboveground biomass of global forests. Remote Sens. 8, 522. https://doi.org/10.3390/rs8060522.

Zhang, Y., Zhou, S., Gentine, P., Xiao, X., 2019. Can vegetation optical depth reflect changes in leaf water potential during soil moisture dry-down events? Remote Sens. Environ. 234, 111451 https://doi.org/10.1016/j.rse.2019.111451.